J. Cent. South Univ. (2021) 28: 1155−1169
DOI: https://doi.org/10.1007/s11771-021-4687-9

Springer

Interface microstructure and mechanical properties of selective laser melted multilayer functionally graded materials

WANG Di(王迪)[1], DENG Guo-wei(邓国威)[1], YANG Yong-qiang(杨永强)[1],
CHEN Jie(陈杰)[1], WU Wei-hui(吴伟辉)[2], WANG Hao-liang(王皓亮)[3], TAN Chao-lin(谭超林)[1]

1. School of Mechanical and Automotive Engineering, South China University of Technology, Guangzhou 510640, China;
2. School of Intelligent Engineering, Shaoguan University, Shaoguan 512005, China;
3. School of Mechanical Engineering, Dongguan University of Technology, Dongguan 523830, China

Abstract: Functionally graded material (FGM) can tailor properties of components such as wear resistance, corrosion resistance, and functionality to enhance the overall performance. The selective laser melting (SLM) additive manufacturing highlights the capability in manufacturing FGMs with a high geometrical complexity and manufacture flexibility. In this work, the 316L/CuSn10/18Ni300/CoCr four-type materials FGMs were fabricated using SLM. The microstructure and properties of the FGMs were investigated to reveal the effects of SLM processing parameters on the defects. A large number of microcracks were found at the 316L/CuSn10 interface, which initiated from the fusion boundary of 316L region and extended along the building direction. The elastic modulus and nano-hardness in the 18Ni300/CoCr fusion zone decreased significantly, less than those in the 18Ni300 region or the CoCr region. The iron and copper elements were well diffused in the 316L/CuSn10 fusion zone, while elements in the CuSn10/18Ni300 and the 18Ni300/CoCr fusion zones showed significantly gradient transitions. Compared with other regions, the width of the CuSn10/18Ni300 interface and the CuSn10 region expand significantly. The mechanisms of materials fusion and crack generation at the 316L/CuSn10 interface were discussed. In addition, FGM structures without macro-crack were built by only altering the deposition subsequence of 316L and CuSn10, which provides a guide for the additive manufacturing of FGM structures.

Key words: selective laser melting; multilayer functionally graded material; interfacial characterization; crack defects; mechanical properties

Cite this article as: WANG Di, DENG Guo-wei, YANG Yong-qiang, CHEN Jie, WU Wei-hui, WANG Hao-liang, TAN Chao-lin. Interface microstructure and mechanical properties of selective laser melted multilayer functionally graded materials [J]. Journal of Central South University, 2021, 28(4): 1155−1169. DOI: https://doi.org/10.1007/s11771-021-4687-9.

1 Introduction

With the increasing demand for functionally graded materials (FGMs) in the fields such as aerospace, defense and biomedicine, many scholars have committed to manufacturing FGM structures through additive manufacturing techniques [1−5]. Selective laser melting (SLM) is a typical metal additive manufacturing technology that fabricates components with complex structures by laser melting and consolidating powder particles layer-by-layer. Compared with other metal additive manufacturing technologies, SLM has the

Foundation item: Project(2020B090922002) supported by Guangdong Provincial Key Field Research and Development Program, China; Projects(51875215, 52005189) supported by the National Natural Science Foundation of China; Project(2019B1515120094) supported by Guangdong Provincial Basic and Applied Basic Research Fund, China
Received date: 2020-11-29; **Accepted date:** 2021-03-11
Corresponding author: TAN Chao-lin, PhD, Research Fellow; Tel: +86-13570943211; E-mail: tclscut@163.com; ORCID: https://orcid.org/0000-0003-2029-4600

advantages of high dimensional accuracy and low roughness [6−9]. Additionally, compared with traditional manufacturing technologies, such as casting and welding, SLM can not only fabricate components with complicated shapes and flexible material constitutions, but also reduce lead time, and material costs.

FGM structure can apply appropriate materials in different areas of a component to configure the required properties in localized positions of a component [10]. At present, a number of scholars have succeeded in fabricating some complex-shaped FGM structures through SLM [11−14]. However, there are still some problems with the SLM process for fabricating FGM structures, such as the tendency of cracks occurrence at the heterogeneous material interface. MEI et al [15] found a great many cracks at the interface of 316L/In718 bimetallic structure and the formation of these cracks may be related to the thermal properties of materials [16]. CHEN et al [17] proposed a multi-layer finite element model to study the intricate thermodynamic behavior of the interface of Ti6Al4V/TiB_2 bimetallic structure under different process parameters. The results indicated that the maximum temperature gradient is at the interface between the Ti6Al4V and TiB_2 layers, causing great thermal stress which will further lead to the formation of thermal cracks and deformations at the interface when the stress is released [18]. Obviously, the thermal properties of materials have an important influence on the interface performance of FGM structures. In addition, it is likely to form a brittle phase at the interface, thus weakening the interface performance of FGM structures [19, 20].

The weak interface performance limits the practical application of FGM structures, which has forced some scholars to conduct studies to explore methods of improving the interface performance. Some studies [13, 21] demonstrated that the energy input is closely linked to the building quality of the heterogeneous material interface. Proper energy input can reduce the formation of pores, cracks and other defects at the interface, thereby enhancing the interface performance. In addition to controlling the energy input, the same purpose can be achieved by adopting the appropriate methods to build the heterogeneous material interface. Up to now, there are three methods of combining different materials to build the heterogeneous material interface, including the direct combination method [22], the composition transition method [13] and the interlayer bonding method [23]. Moreover, the use of remelting strategy and some special designs for heterogeneous material interface structure can also help to improve the interface performance. KOOPMANN et al [24] utilized the remelting effect of a high-power laser to create a jagged surface between the steel layer and ceramic layer, which significantly improved the bonding between steel and ceramic. WEI et al [25] designed a jagged interface structure to acquire good metallurgical bonding at the interface. TAN et al [26] enhanced bonding strength of the FGM through an in-situ formed interlayer. Although many studies on enhancing interface performance have been conducted, there is a lack of in-depth research to reveal the mechanism of material fusion and defect generation at the interface. Only when the mechanism of material fusion and defect formation at the interface is clearly understood, can the interface performance be effectively improved to enable the application of FGM structures in real industrial contexts.

This study was carried out on a self-developed multi-material SLM equipment, by which the 316L/CuSn10/18Ni300/CoCr FGM structure was fabricated. The studies by ZHANG et al [27] and CHEN et al [28] offered a reference for the study. This study focused on the SLM fabrication of FGM using four different materials, followed by characterizations of interfacial microstructure and mechanical properties. In addition, the mechanisms of material fusion and defect formation at the interface were discussed.

2 Experimental

2.1 Materials

The materials used in the experiment were CoCr (Material Technology Innovations Co., Ltd., China), 18Ni300 (AVIMETAL PM, China), CuSn10 (Dongguan Jingyan Technology Development Co., Ltd., China) and 316L powder (Changsha Hualiu Metallurgy Powder Co., Ltd., China). The composition of these powders is shown in Table 1. These materials were chosen for the study because their SLM process is relatively mature, and each of them has critical applications in different fields. For example, 316L is widely used in industrial production and daily life. CuSn10 has good wear and

Table 1 Composition of CoCr, 18Ni300, CuSn10 and 316L powder

Powder	Composition/wt.%									
CoCr	Co	Cr	Mo	Si	Ni	Fe	Mn	C	O	
	28.62	65.07	5.49	<1.5	<1.0	<0.75	<1.0	<0.15	<0.10	
18Ni300	Ni	Co	Mo	Mn	Si	S	Cr	Cu	O	Fe
	17.49	8.48	4.77	0.044	0.062	0.002	0.1	0.013	0.013	Bal.
CuSn10	Cu	Sn	P	Ni	Pb	Fe	Zn	Al	Cr	Si
	88.52	10.61	0.79	0.0077	0.0059	0.0048	0.0036	<0.001	<0.001	<0.001
316L	Cr	Ni	Mo	Si	Mn	C	S	P	O	Fe
	17.85	13.04	2.62	1.17	0.17	0.008	0.002	0.003	0.065	Bal.

corrosion resistance and is used in wear-resistant parts, such as oiled bearings and diamond tools. 18Ni300 has important applications in the molds because of its ultra-high strength and good toughness. CoCr has important applications in the field of dentistry due to its good biocompatibility. FGM made from these materials will make full use of their advantages and be used more widely in the fields such as automotive, marine and construction machinery.

2.2 Multi-material SLM equipment and processing

The experiment was carried out on Dimetal-100 SLM equipment (South China University of Technology, China) with the schematic diagram of the equipment shown in Figure 1. The equipment is mainly composed of a 500W fiber laser (YLR-500-WC, IPG), optical transmission regulation system, gas circulation system, building chamber, powder feeding device, cooling system, and the main control software. The laser is guided by a high-precision optical path transmission system, and it is basically the same throughout the working plane. The maximum fabricating dimensions of the equipment are 100 mm × 100 mm × 100 mm, the scanning speed is 10−7000 mm/s, the focused spot diameter is 70 μm, and the precision can reach ±0.1 mm. However, unlike other conventional SLM devices, the equipment includes four sets of powder feeding devices, adopting a method of feeding powders from top to bottom. The powder feeding devices are installed outside the building chamber, which enables the powder to be added during the SLM forming process. Moreover, the powder feeding speed of each powder tank is monitored and controlled by a powder flow regulator. There are four powder hoppers on the laying car, each of which has

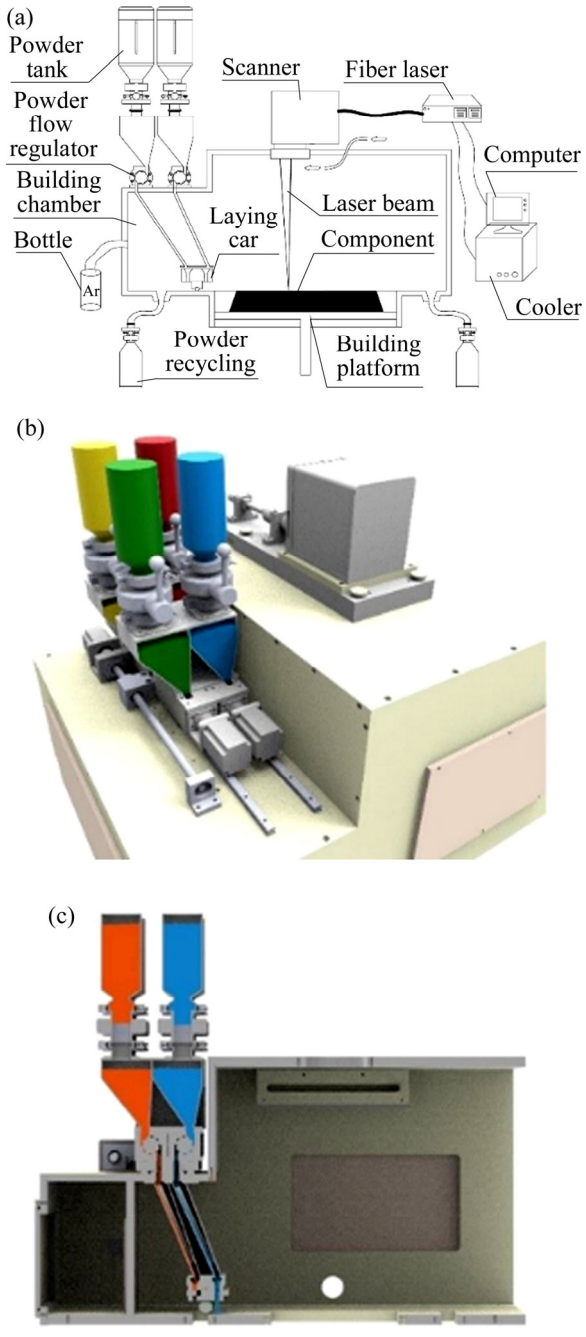

Figure 1 Dimetal-100 SLM equipment: (a) Schematic diagram; (b, c) Three-dimensional model

a switch that controls the distribution of four kinds of powder at diverse positions.

Steel-copper bimetallic parts are being widely used in the power generation industry, nuclear industry and automobile industry. Therefore, the combination of steel and copper is the focus of this study, and the combination of 316L/CuSn10 and CuSn10/18Ni300 are set up. For a new attempt, the 18Ni300/CoCr combination was chosen. In addition, steel and copper differ significantly in thermal expansion. Hence, it is worth investigating whether their deposition sequences affect the formation of interface defects. Therefore, the four materials are deposited in the order of CoCr, 18Ni300, CuSn10 and 316L. The FGM samples were fabricated by the following method. First, the CoCr powder was melted and then deposited on the substrate to build a CoCr region. After building the CoCr region, the tank of CoCr powder stopped feeding powder while tank of 18Ni300 powder began feeding powder, but it should be noted that the building platform must be kept in place during the process. However, before starting the normal building process, in order to form a metallurgical bonding between the CoCr region and the 18Ni300 region, the equipment performed laser scanning without spreading powder three times using laser parameters of melting the CoCr powder, and then it performed laser scanning with spreading powder twice using laser parameters of melting the 18Ni300 powder. During the above laser scanning, the building platform was still kept in place. Then the 18Ni300 region was normally built. The tank of 18Ni300 powder stopped working, and the tank of another powder started feeding powder. Repeat the above process until FGM samples were fabricated. The process parameters of FGM samples are shown in Figure 2. Each single-alloy region was built according to different SLM process parameters, and an island scanning strategy (single rectangular square area of 5 mm×5 mm) was adopted during the process. Island scanning strategy can reduce the temperature gradient during the SLM process, thereby reducing the residual stress and ensuring the smooth building of the FGM samples [29].

2.3 Characterization of microstructure and performance

After the metallographic samples were prepared on the basis of standard procedure, their interfacial microstructure was observed by a metallographic

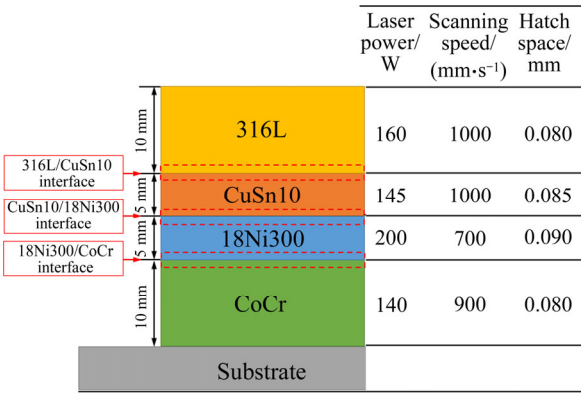

Figure 2 Schematic diagram of FGM sample

microscope (Leica, DM4M) and a scanning electron microscope (ZEISS, Sigma 500). Energy spectrum analyses of each interface were conducted by an energy spectrum analyzer (Oxford instrument, X-Max Extreme). Vickers microhardness was measured on polished samples by a Vickers hardness tester (Buehler, 402MVD) under the load of 1.96 N. The microhardness of each interface was measured three times, and then characterized by the average of three measured values. The nanoindentation experiment was carried out on a nano-indenter (Agilent, Nano Indenter G200) to obtain the elastic modulus and the nano-hardness in the diverse place of samples. As shown in Figure 3, the test sample of nanoindentation experiment was a solid rectangular block with a thickness of about 4.1 mm and a length of about 28.6 mm. The measuring areas were three interface areas of the sample, including the first interface (the 316L/CuSn10 interface), the second interface (the CuSn10/18Ni300 interface) and the third interface (the 18Ni300/CoCr interface).

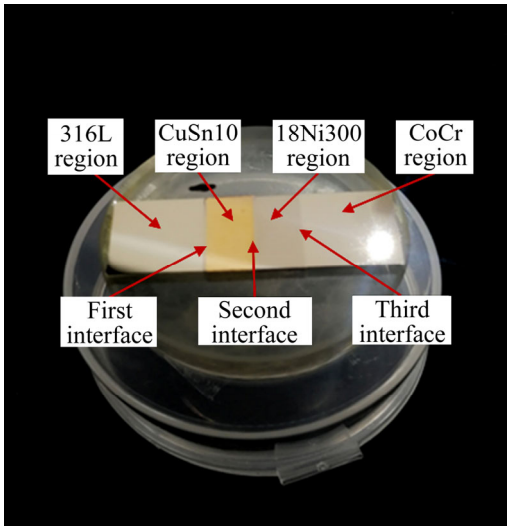

Figure 3 Sample for nanoindentation testing

Twenty-five points were measured along the interface, and the distance between two points was 50 μm. The loading force was set as 500 mN, and duration time was 5 s.

3 Results and discussions

3.1 Microstructure

Figure 4 shows the macro-morphologies of the SLM-processed FGM samples, which demonstrates the good built quality of samples. Figure 5 shows that there are no obvious defects except for cracks at a specific interface. Cracks were generated at the 316L/CuSn10 interface while both the CuSn10/18Ni300 interface and the 18Ni300/CoCr interface had a good metallurgical bonding without visible cracks. Figure 5(a) illustrates that cracks with lengths of 2509 μm and 843 μm formed at both ends of the 316L/CuSn10 interface, but the middle part was well bonded without cracks. During the SLM

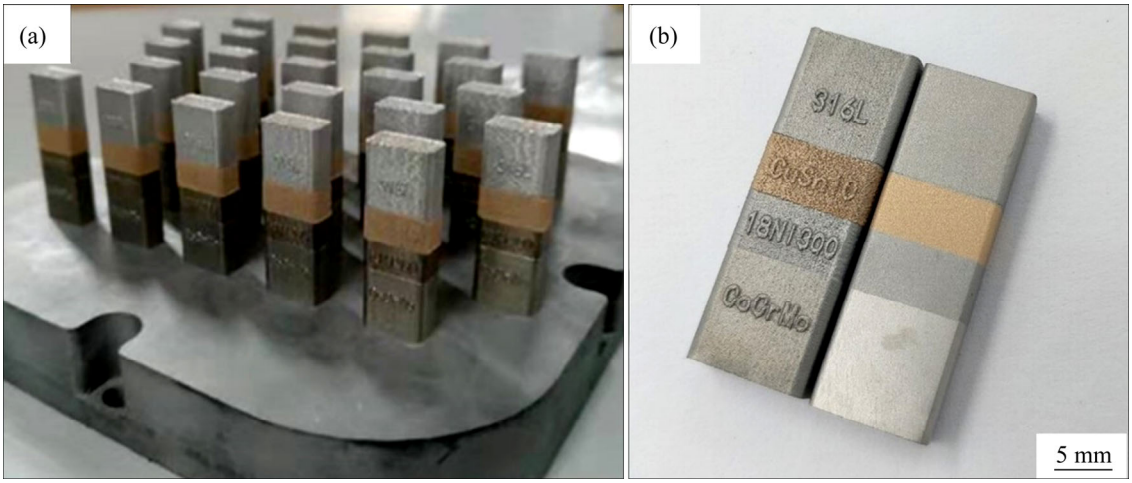

Figure 4 Photos showing SLM-processed FGM samples

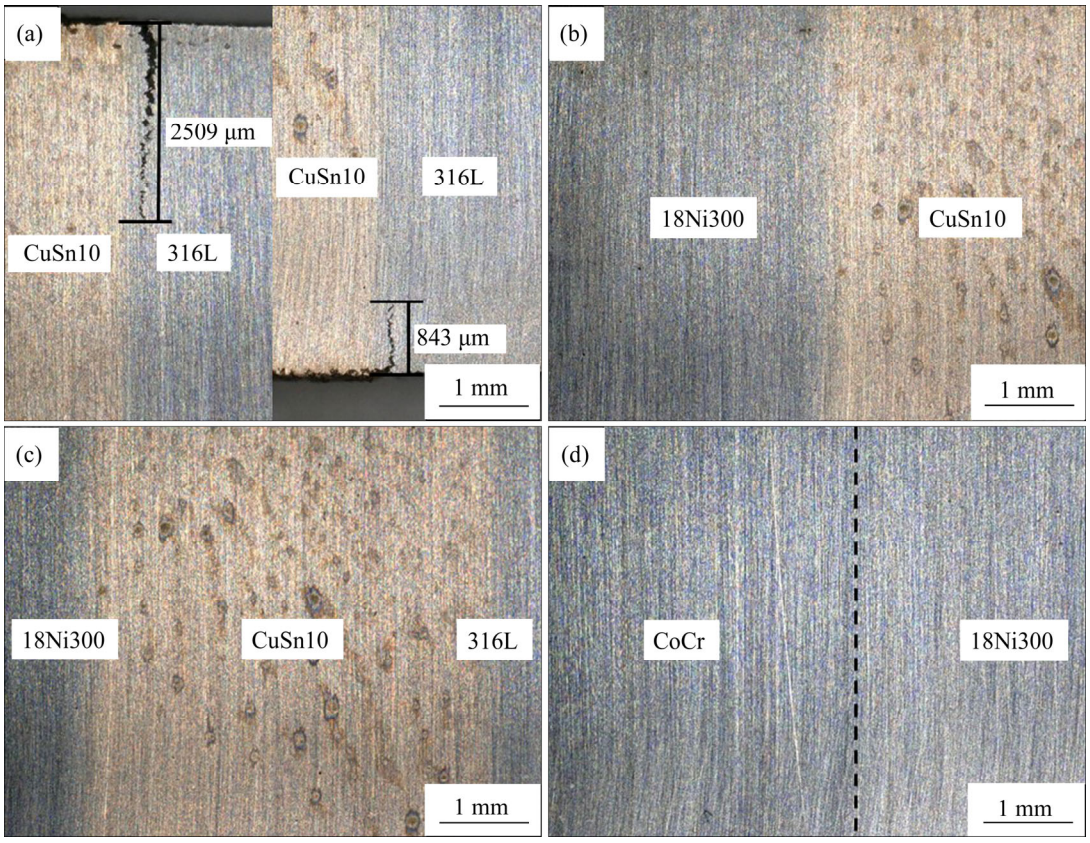

Figure 5 OM images of different interface of SLM-processed FGM: (a) 316L/CuSn10 interface; (b) CuSn10/18Ni300 interface; (c) 316L/CuSn10/18Ni300 interface; (d) 18Ni300/CoCr interface

process, the built parts will gradually accumulate heat as new layers continue to be deposited. However, the high thermal conductivity of copper enables the 316L part near the 316L/CuSn10 interface to cool down fast. Shrinkage stresses caused by rapid cooling caused the warpage effect at the 316L/CuSn10 interface [30]. Hence, the cracks are more severe at the edge. In addition, the boundary of 18Ni300/CoCr interface in Figure 5(d) is not distinct.

Figure 6 shows the interface microstructure of FGM samples. At the 316L/CuSn10 interface, microcracks were found in the 316L region near the fusion zone, and a large number of pores occurred in the CuSn10 region. At the CuSn10/18Ni300 interface, there were many pores in the CuSn10 region but a few pores in the 18Ni300 region near the fusion zone. At the 18Ni300/CoCr interface, no crack or pore but continuous and well adherent interface was found. The pores were not concentrated in the fusion zone but were distributed evenly through the CuSn10 region. Therefore, these pores might be caused by the inappropriate laser parameters for the CuSn10 region. During the SLM fabrication of 316L/CuSn10 bimetallic structure, CHEN et al [28] built the CuSn10 part without pores using the laser parameter with a power of 300 W, a scanning speed of 700 mm/s, a hatch space of 0.085 mm and a layer thickness of 0.03 mm (laser volume energy density 168 J/mm^3). In contrast, the laser parameter (laser power 145 W, scanning speed 1000 mm/s, hatch space 0.085 mm, layer thickness 0.03 mm, laser volume energy density 57 J/mm^3) for the CuSn10 region in this research caused insufficient laser energy input, resulting in irregular-shaped pores due to the poor interlayer bonding. Moreover, insufficient laser energy input made the solidification process too transitory to release the gas dissolved in the molten pool. The gas did not escape from the molten pool before solidification. Thus, small pores with an approximately spherical shape formed. The formation of the pores that occurred in the 18Ni300 region near the interface was similar. When CuSn10 was deposited on 18Ni300, the laser remelted the upper layer of the 18Ni300 region. Due to low laser energy input, the solidification process was so transitory that dissolved gas could not escape from the molten pool and then caused the formation of spherical pores. A large number of microcracks that were present in the 316L region near the interface might be caused by the mismatch of the thermal properties between 316L and CuSn10. The detailed formation process of these cracks will be discussed in the following discussion.

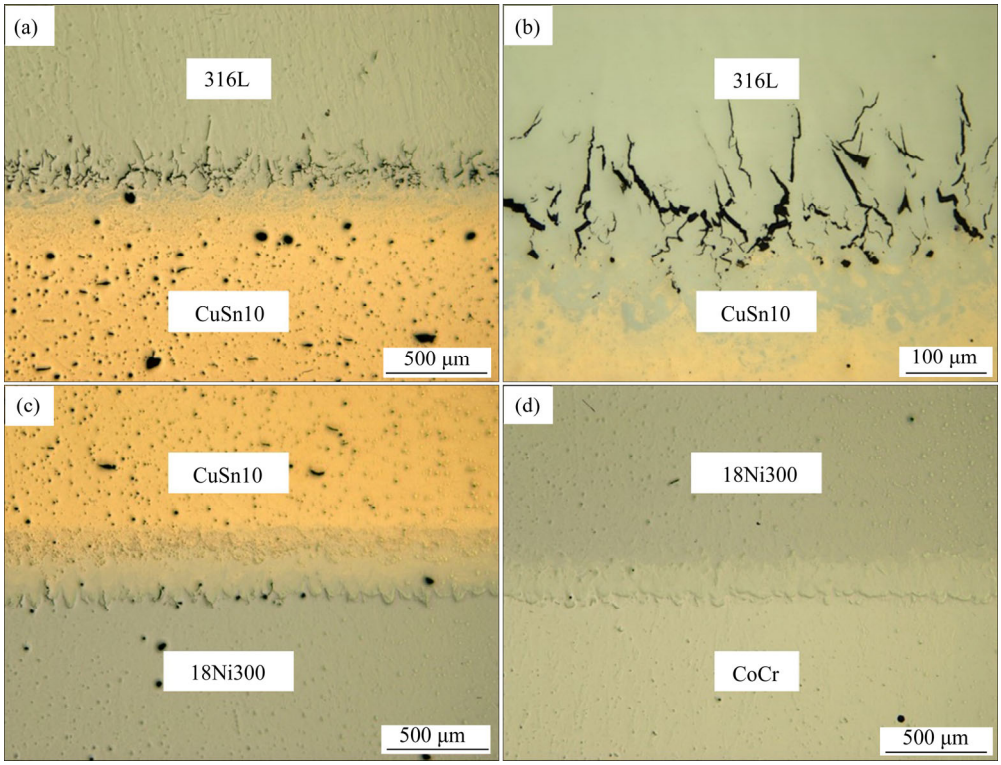

Figure 6 Metallographic fusion of heterogeneous material interfaces: (a, b) 316L/CuSn10 interface; (c) CuSn10/18Ni300 interface; (d) 18Ni300/CoCr interface

3.2 Microhardness

The Vickers microhardness at the three interfaces of the FGM structure is shown in Table 2. The hardness of the second interface (the CuSn10/18Ni300 interface) is between the hardness of the two materials that constitute the heterogeneous material interface. The hardness of the first interface (the 316L/CuSn10 interface) exceeds that of 316L and CuSn10, while the hardness of the third interface (the 18Ni300/CoCr interface) is lower than that of CoCr and 18Ni300. Therefore, new intermetallic phases may be formed at the first interface and the third interface, which can affect the hardness. In addition, Figure 7 shows the change of Vickers microhardness along the building direction. Since different materials have diverse hardness, the Vickers microhardness curve rises and falls. Among the four materials used in this study, 18Ni300 has the highest Vickers microhardness while CuSn10 has the lowest Vickers microhardness.

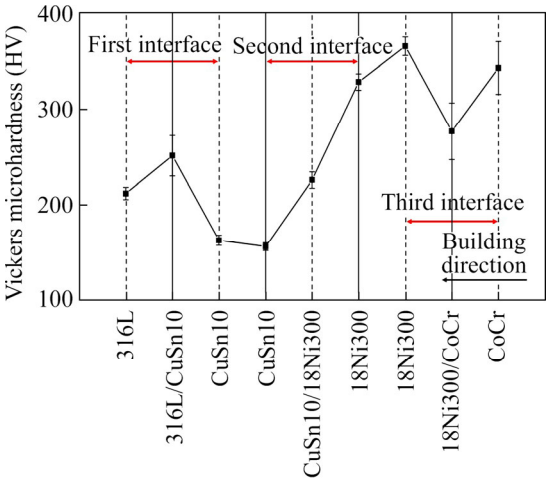

Figure 7 Vickers microhardness curve of FGM along the building direction

3.3 Nanoindentation and performance characterization

At the first interface, from the 316L region to the CuSn10 region, the general trend of the elastic modulus is to increase slowly, then sharply decrease and tend to be stable after the 19th measuring point, as shown in Figure 8(c). At the 13th measuring point, which is on the interface between the two materials, the elastic modulus reaches its maximum value. The elastic modulus values at the 10th, 11th and 12th measuring points, which suddenly decrease because these points are close to cracks, cannot characterize the mechanical properties of the material. As shown in Figure 8(d), the general trend of the nano-hardness is similar to that of the elastic modulus. It first rises slowly, then drops sharply, and gradually stabilizes. The nano-hardness reaches its maximum value at the 14th measuring point and minimum value at the 10th measuring point. However, the 10th measuring point is near cracks so that its nano-hardness is significantly lower than the normal value and cannot characterize the mechanical properties. It can be seen that cracks will affect the elastic modulus and nano-hardness of their adjacent areas to far below the normal value, thus weakening the macro mechanical properties of the sample. In addition, the nano-hardness of the fusion zone obviously exceeds those of the 316L and the CuSn10 region, so it can be inferred that a new intermetallic phase may form between 316L and CuSn10. The EDS analysis of the first interface is shown in Figure 9. It can be seen that

Table 2 Vickers microhardness at interface of FGM samples

Interface	Measurement position	Data 1 (HV)	Data 2 (HV)	Data 3 (HV)	Average (HV)	Standard deviation (HV)
First interface	316L(About 500 μm away from the first interface)	207. 1	210. 1	219. 3	212.2	6.4
	316L/CuSn10 interface	274. 1	248. 5	232. 3	251.6	21.1
	CuSn10(About 500 μm away from the first interface)	163. 7	168. 6	158. 3	163.5	5.2
Second interface	CuSn10(About 500μm away from the second interface)	152. 4	158. 1	160. 2	156.9	4.0
	CuSn10/18Ni300 interface	216. 5	231. 3	231. 2	226.3	8.5
	18Ni300(About 500 μm away from the second interface)	319. 3	336. 0	330. 6	328.6	8.5
Third interface	18Ni300(About 500 μm away from the third interface)	375. 4	365. 5	356. 2	365.7	9.6
	18Ni300/CoCr interface	311. 2	259. 0	261. 2	277.1	30.0
	CoCr(About 500 μm away from the third interface)	358. 8	311. 1	359. 0	343.0	27.6

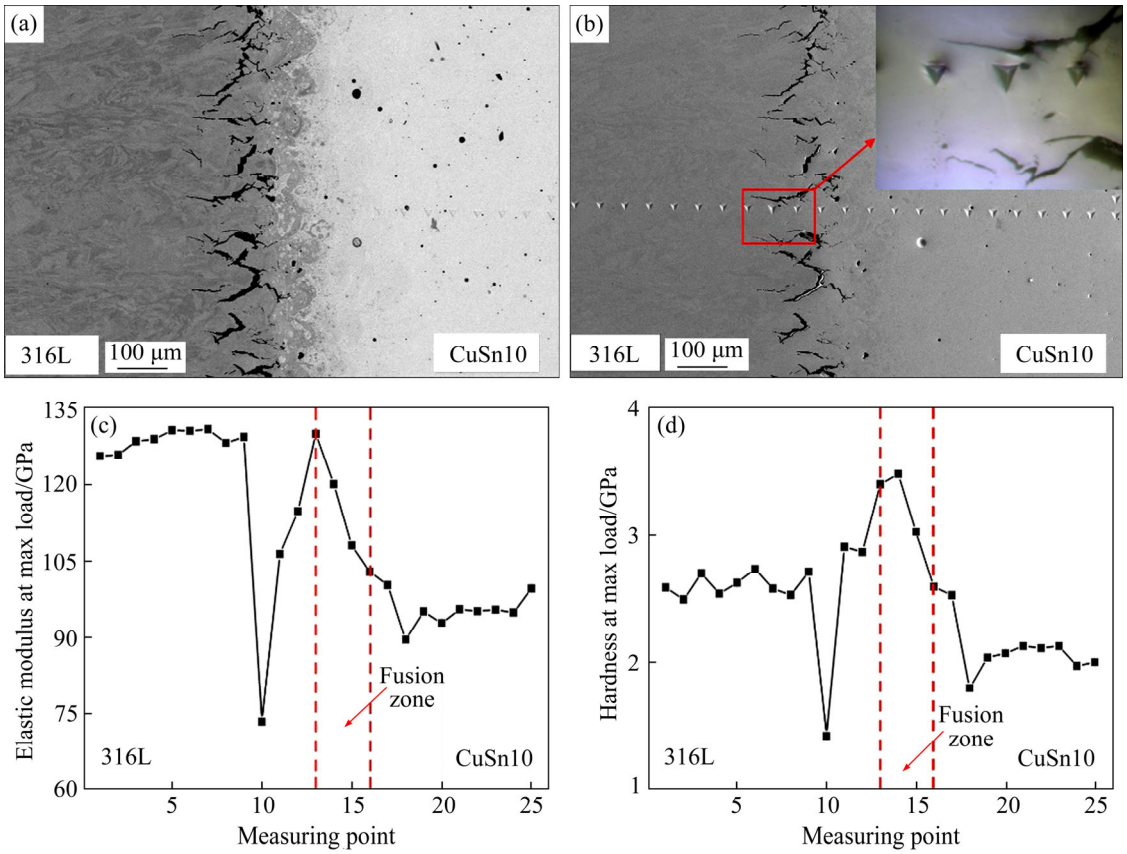

Figure 8 Microscopic characteristics and performance characterisation of first interface: (a) Backscatter image; (b) Secondary electron image; (c) Elastic modulus curve; (d) Nano-hardness curve

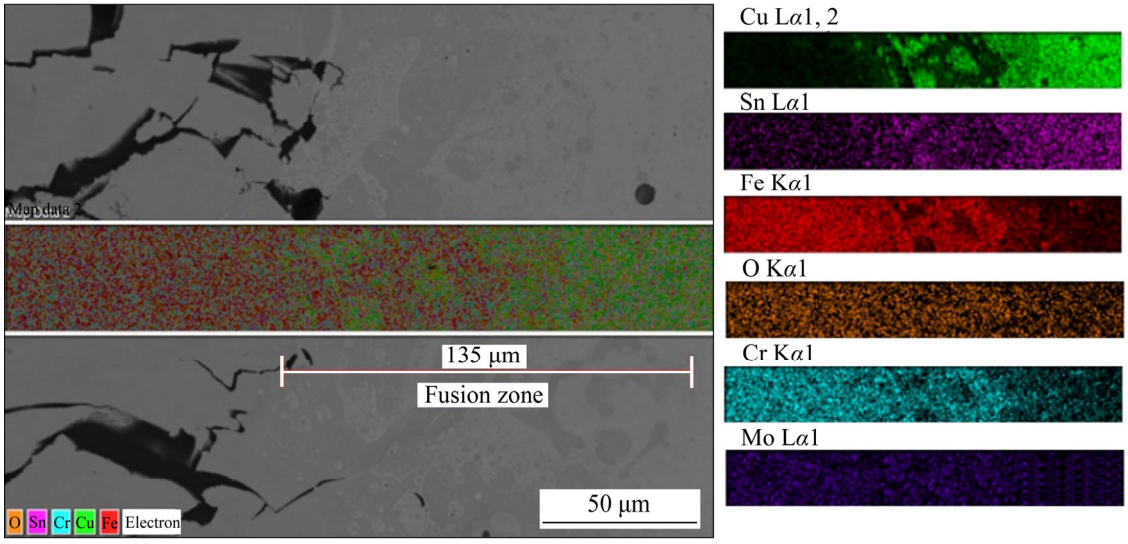

Figure 9 EDS mapping analysis at 316L/CuSn10 interface

the width of the fusion zone is approximately 135 μm. In the fusion zone, both iron element and copper element have sufficient diffusion which enables the 316L/CuSn10 interface to have good joint strength. Enhancing the diffusion of elements at the interface contributes to obtaining better interfacial bonding [25].

The measuring point marked by a red circle in Figures 10(a) and (b) is used to help determining the interface, and its elastic modulus and nano-hardness are not adopted. At the second interface, from the CuSn10 region to the 18Ni300 region, the general trend of the elastic modulus is to increase slowly and then sharply increase, as shown in Figure 10(c). The

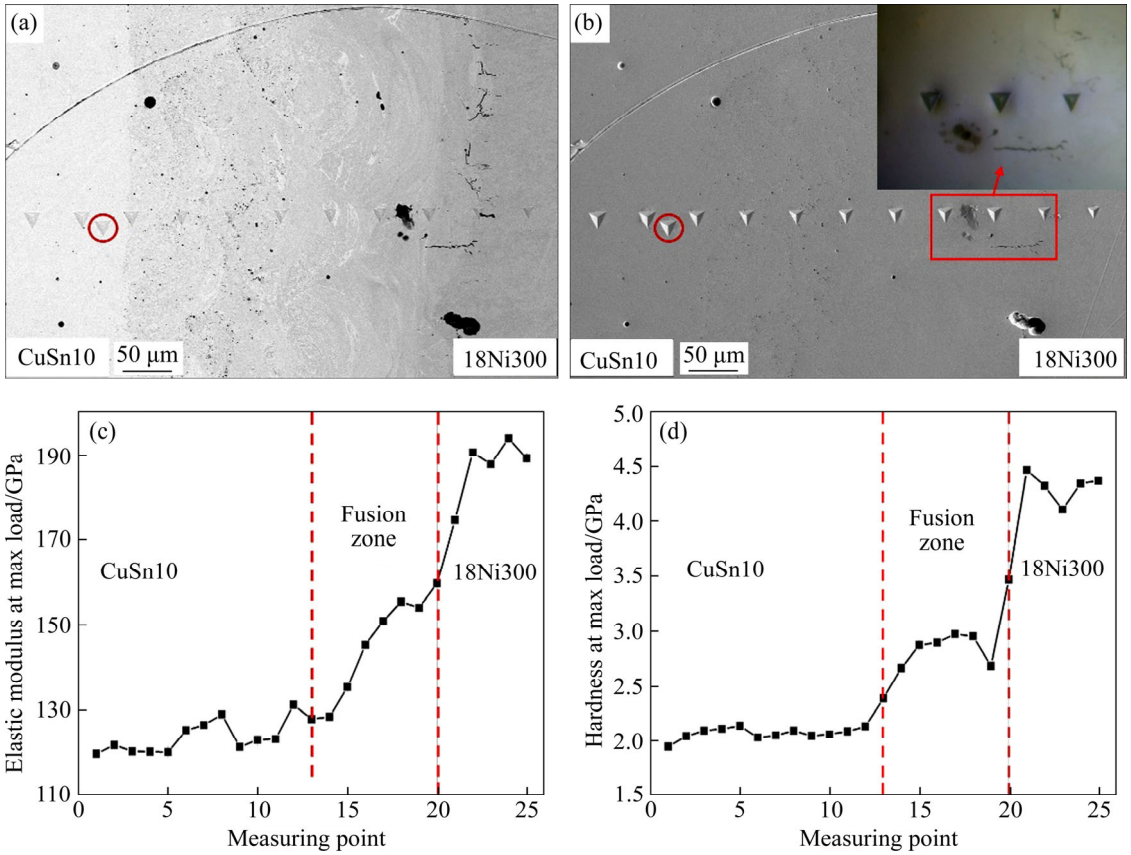

Figure 10 Microscopic characteristics and performance characterisation of the second interface: (a) Backscatter image; (b) Secondary electron image; (c) Elastic modulus curve; (d) Nano-hardness curve

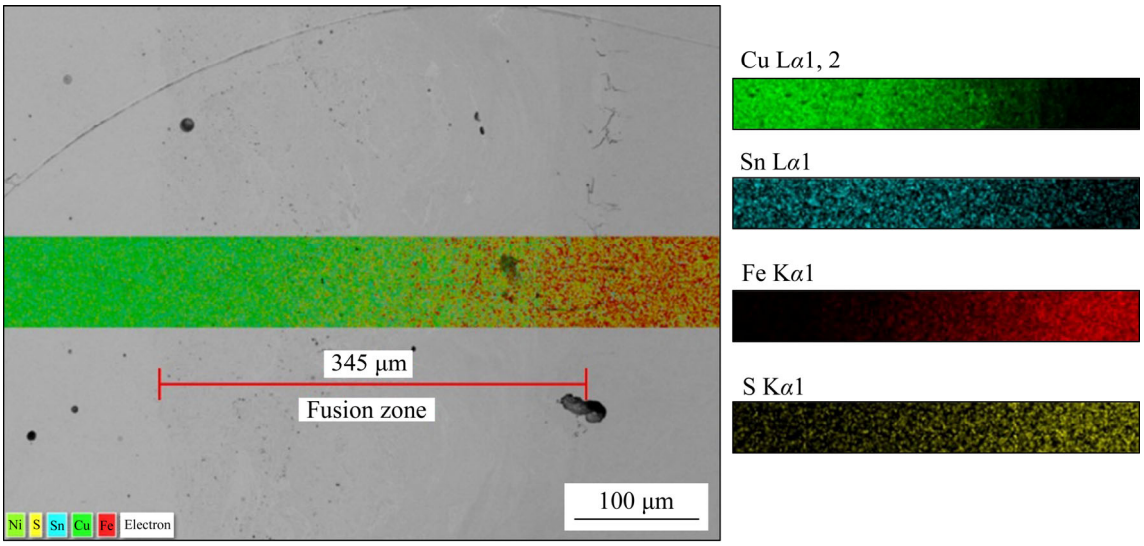

Figure 11 EDS mapping analysis on CuSn10/18Ni300 interface

growth rate of the elastic modulus curve starts to increase dramatically at the 15th measuring point, and the curve reaches the maximum value at the 24th measuring point. The nano-hardness curve has the same trend as the elastic modulus curve, reaching the maximum value at the 21th measuring point, as shown in Figure 10(d). The nano-hardness of the 19th measuring point decreases obviously because the point is close to cracks. Moreover, the nano-hardness in the adjacent area of the CuSn10/18Ni300 interface shows a gradient transition, which is beneficial to reduce the residual stress and improve the interfacial bonding strength [31]. The EDS analysis of the second interface in Figure 11 shows a

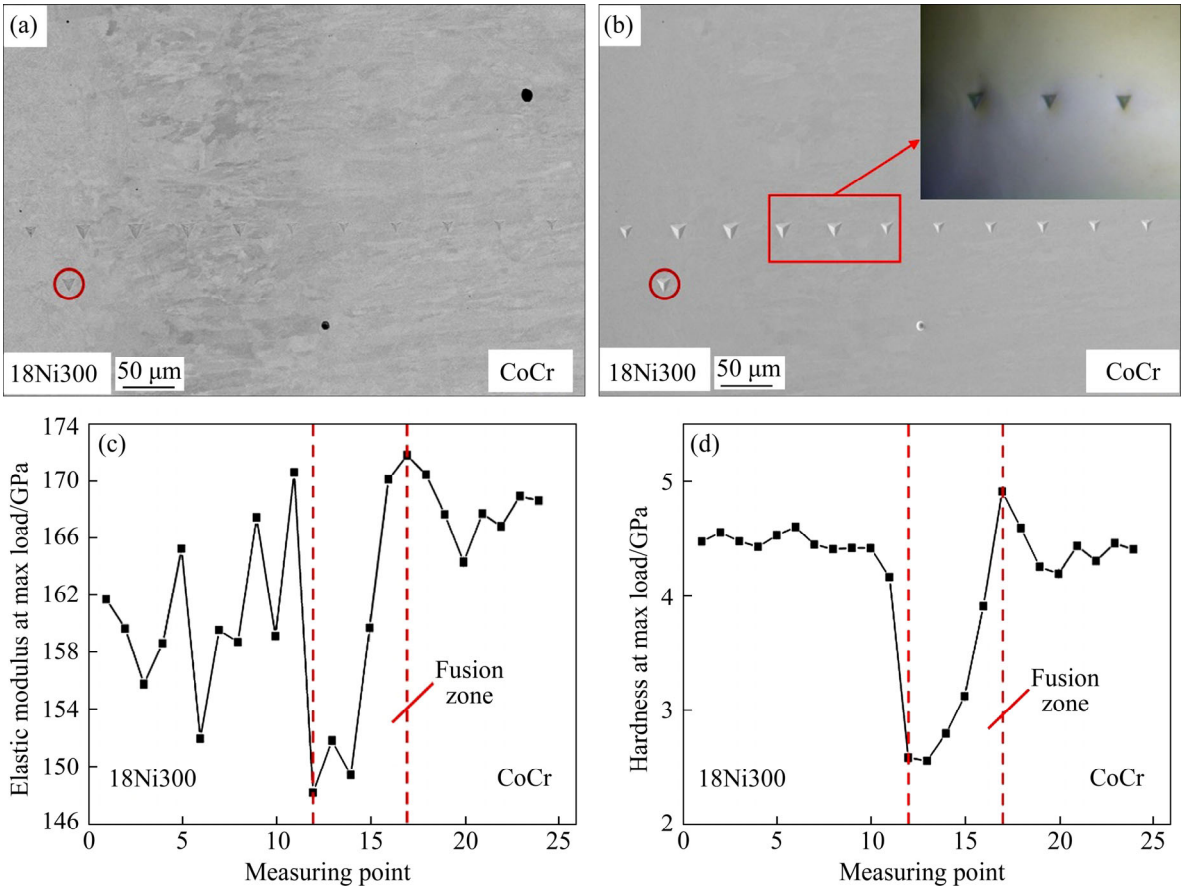

Figure 12 Microscopic characteristics and performance characterization of the third interface: (a) Backscatter image; (b) Secondary electron image; (c) Elastic modulus curve; (d) Nano-hardness curve

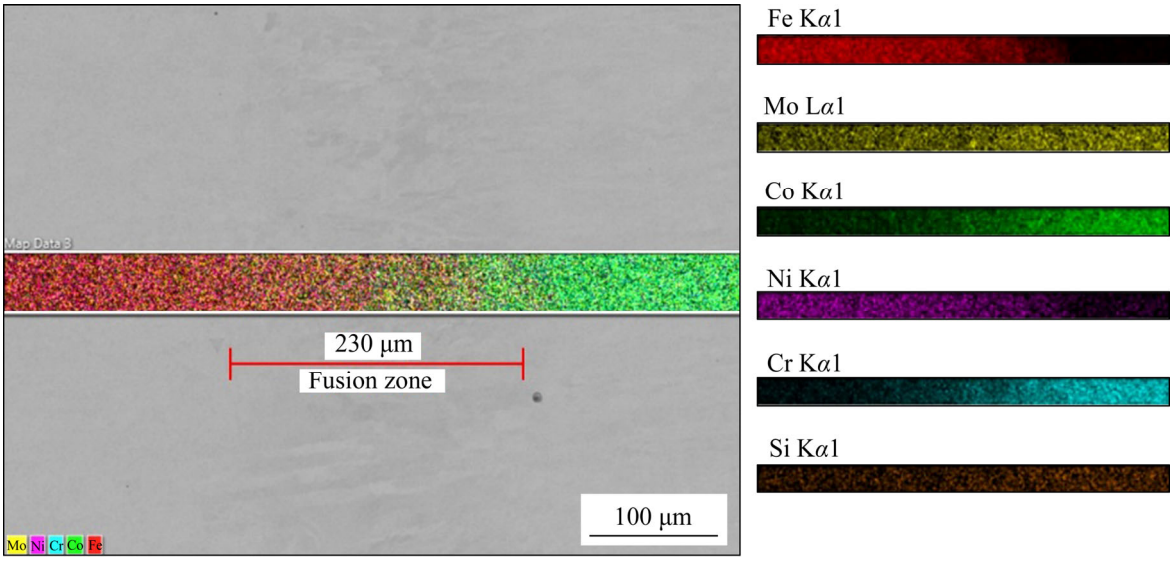

Figure 13 EDS mapping analysis on 18Ni300/CoCr interface

broad fusion zone with a width of 345 μm. In the fusion zone, the content of each metal element gradually transforms. It was reported that the gradient transition of composition is helpful to enhance the interfacial bonding strength [32].

The point circled in red in Figures 12(a) and (b) is the 25th measuring point, but it is used to identify the interface and its data are not adopted. At the third interface, from the 18Ni300 region to the CoCr region, the elastic modulus curve in Figure 12(c)

does not have an obvious trend. In the 18Ni300 region, the elastic modulus rises and falls significantly. When transforming from the 18Ni300 region to the fusion zone, the elastic modulus curve abruptly falls and reaches the minimum value at the 12th measuring point. The elastic modulus curve in the fusion zone rises generally and reaches the maximum value at the 17th measuring point, while that in the CoCr region is in slow decline and tends to be stable. The nano-hardness curve has the same trend as the elastic modulus curve but it remains stable in the 18Ni300 region. It is interesting that the elastic modulus and the nano-hardness in the fusion zone both are significantly are inferior to those in of the 18Ni300 region and the CoCr region. There are no distinct defects in the fusion zone but its mechanical properties are significantly weakened. Therefore, the mechanical properties of this area need further study in future research. The EDS analysis of the third interface is shown in Figure 13, and it can be seen that the width of the fusion zone is approximately 230 μm and the content of each metal element in the fusion zone shows a gradient change.

3.4 Thermal expansion effect

The actual size of the sample after complete cooling was measured, and the expansion increment in the x and y-axis directions was obtained by subtracting the model size from the actual size without regard to the building error of the SLM equipment. Figure 14(a) shows the schematic diagram of the direction, and the result of the expansion increment is shown in Figure 14(b). It can be seen from the expansion increment curve that each region of the FGM sample has a consistent expansion increment in the x- and y-axis directions. Particularly, the expansion increment of the CuSn10 region is much higher than those of other regions. Moreover, the expansion increment of the CuSn10/18Ni300 interface is similar to that of the CuSn10 region, while the expansion increment of the 316L/CuSn10 interface is much smaller than that of the CuSn10 region. This phenomenon indicates that the building order of different materials will affect the thermal expansion effect of the heterogeneous material interface. The heterogeneous material interface formed by depositing CuSn10 material on other materials has the same expansion increment as the CuSn10 region, but the heterogeneous material interface formed by depositing other materials on CuSn10 material does not. The latter building order may not be able to release residual stress through expansion, thereby accumulating large residual stress during the SLM process and leading to the formation of cracks. Therefore, if the material with high thermal expansion coefficient is set as the last material to deposit, FGM samples may avoid the formation of cracks because it may not accumulate an excess of residual stress during the fabricating process.

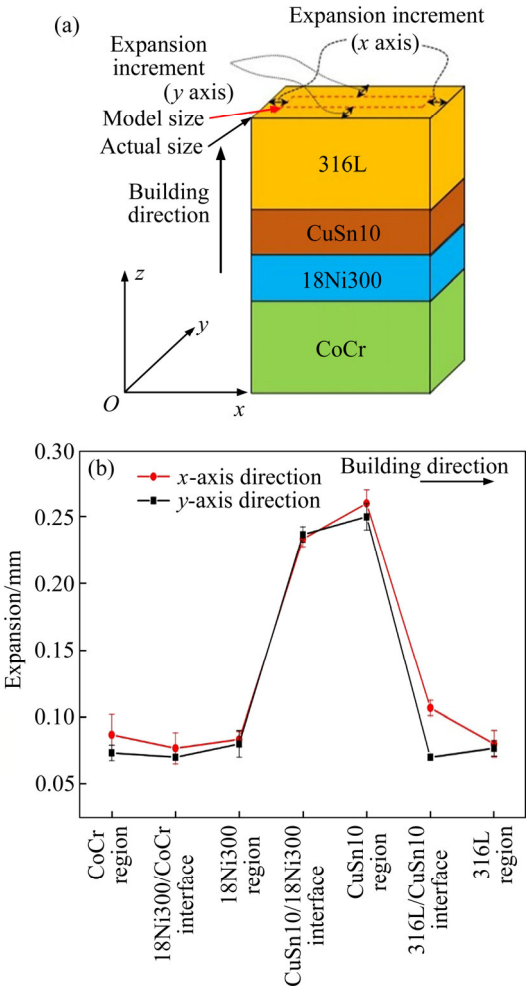

Figure 14 Expansion effect in different directions: (a) Direction diagram; (b) Expansion curves in different regions

3.5 Material fusion and defect formation

As shown in Figure 15(a), 316L infiltrates into the CuSn10 region when depositing 316L on the CuSn10 region, and then the fusion zone forms which composes of CuSn10 and 316L. The 316L region near the fusion zone is also infiltrated by a small amount of CuSn10. Moreover, the boundary (red dotted line in Figure 15(a)) between the fusion

zone and the 316L region is quite irregular. Such fusion results can be explained by the Marangoni convection effect. The circular flow in the molten pool caused by Marangoni convection effect can be observed in the red box of Figure 15(b). Marangoni convection is driven by surface tension induced by a temperature gradient so that a larger temperature gradient will aggravate the Marangoni convection [33]. The high thermal conductivity of copper leads to an increase in the temperature gradient, which enhances the Marangoni convection in the fusion zone. The temperature in the center of the molten pool is higher than the boundary temperature, thereby inducing a temperature gradient. This temperature difference causes surface tension towards the boundary of the molten pool. The surface tension pulls the liquid metal toward the boundary of the molten pool while the gravity forces the liquid metal to flow down to the bottom of the molten pool, which induces the circular flow in the molten pool [34]. During the SLM process, high energy laser melted 316L powder and the upper layer of the CuSn10 region to form the molten pool. Under the action of the Marangoni convection, the molten CuSn10 was pulled toward the 316L region and the molten 316L penetrated into the CuSn10 region.

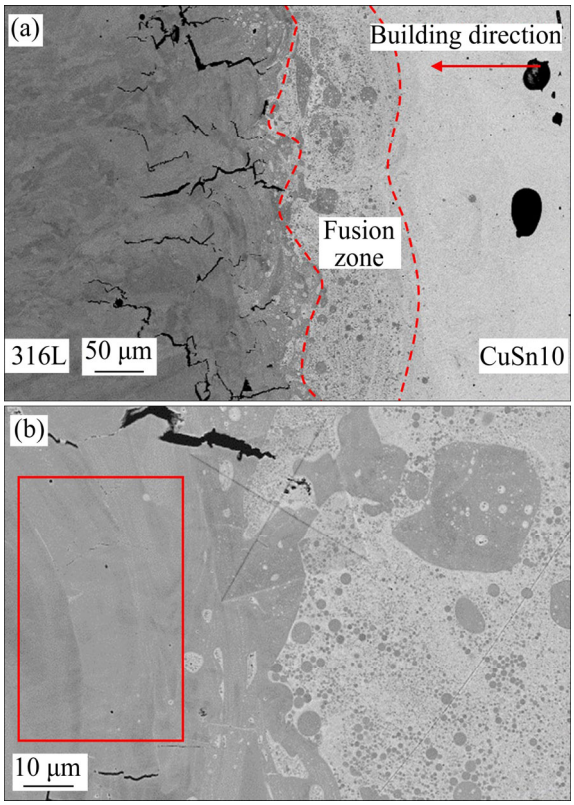

Figure 15 Material fusion and cracks at the 316L/CuSn10 interface

Therefore, the fusion zone in Figure 15 finally formed. Marangoni convection promotes mass transfer between the 316L region and the CuSn10 region to acquire better metallurgical binding.

Noted in Figure 15(a), a large number of microcracks exist in the 316L region, which has adverse effects on the interfacial bonding strength. These microcracks extend from the fusion zone boundary to the 316L region along the build direction. The cracks initiated in the interface due to mismatch of coefficient of thermal expansion (CTE) and mechanical properties between these two materials. With the continuation of 316L deposition, the residual stress in the interface increased, which promoted the cracks expansion towards the 316L region. Moreover, copper diffusion into the austenite grain boundaries made them brittle and promoted the microcracks to form along the stainless steel grain boundary [35]. On the other hand, since the melting point of stainless steel (~1400 °C) is higher than that of copper alloy (~1080 °C) [36], 316L precedes CuSn10 to solidify in the fusion zone. Furthermore, the thermal expansion coefficient of copper is higher than that of steel [37], which easily induces large stress during the deposition of 316L on CuSn10. The post-solidified CuSn10 was constrained by the upper 316L layer and the lower CuSn10 layer and the stress accumulated. However, the stress could not be released by the lower CuSn10 layer that had been completely solidified, but had to be released by the upper 316L layer that was incompletely solidified. The upper 316L layer could not release the stress through shrinkage plastic deformation, so it was torn. In addition, the thermal conductivity of solids is generally higher than that of powders and copper has high thermal conductivity. Therefore, the heat is mainly dispersed through the bottom CuSn10 region when depositing 316L on the CuSn10 substrate. This tends to cause a large temperature gradient between the 316 and the CuSn10 regions, resulting in the formation of large stresses. Finally, the FGM samples without obvious macro-cracks were fabricated by only exchanging the building order of 316L and CuSn10. In this research, the laser energy input of the CuSn10 region was much smaller than those of the 316L region and the 18Ni300 region. Therefore, during the deposition of 316L (or 18Ni300) on CuSn10, the heat accumulated in the fusion zone decreased and induced the smaller

temperature difference, thereby avoiding the large residual stress. Furthermore, CuSn10 with a higher thermal expansion coefficient was subject to fewer constraints during solidification in the fusion zone. It was mainly bound by the lower 316L layer (or the lower 18Ni300 layer), which was beneficial to release the residual stress. Consequently, depositing CuSn10 on 316L or 18Ni300 did not cause the formation of significant cracks, but depositing 316L on CuSn10 did.

4 Conclusions

The 316L/CuSn10/18Ni300/CoCr FGM was fabricated by SLM using optimized process parameters and scanning strategy. The interfacial defects, microstructure, hardness profile, and elastic modulus of FGM were investigated. Main conclusions include:

1) Macro-cracks were only found at the 316L/CuSn10 interface. There were also some microcracks that initiated in the 316L/CuSn10 interface and extended into 316L along the build direction. Some pores formed at the CuSn10/18Ni300 interface, while a good metallurgical bonding formed at the 18Ni300/CoCr interface were observed.

2) The Vickers hardness of the CuSn10/18Ni300 interface was between those of the CuSn10 region and the 18Ni300 region. The Vickers hardness of the 316L/CuSn10 interface exceeded those of the 316L region and the CuSn10 region, while the Vickers hardness of the 18Ni300/CoCr interface was inferior to those of the 18Ni300 region and the CoCr region. Therefore, new phases may have formed at the 316L/CuSn10 interface and the 18Ni300/CoCr interface.

3) At the 316L/CuSn10 interface, the elastic modulus gradually changed from the 316L region to the CuSn10 region. The nano-hardness of the fusion zone was much higher than the 316L region and the CuSn10 region. At the CuSn10/18Ni300 interface, the elastic modulus and the nano-hardness both had the gradient transition. At the 18Ni300/CoCr interface, the elastic modulus and the nano-hardness of the fusion zone significantly decreased and were lower than those of the 18Ni300 region and the CoCr region.

4) The iron and copper elements were well diffused in the fusion zone at the 316L/CuSn10 interface, while each metal element exhibited a significant gradient transition in the fusion zone of the CuSn10/18Ni300 interface and the 18Ni300/CoCr interface. The gradient transition of elements could benefit metallurgical bonding.

5) The CuSn10/18Ni300 interface and the CuSn10 region had a distinct expansion effect due to the high thermal expansion coefficient of copper, but the 316L/CuSn10 interface showed no obvious expansion. This result indicates that the expansion effect of the heterogeneous material interface is related to the building order of different materials. If the material with the high thermal expansion coefficient was set as the last material to deposit, it may reduce the residual stress accumulation during the SLM process, which could avoid the formation of cracks.

Contributors

The overarching research goals were developed by WANG Di, WU Wei-hui and YANG Yong-qiang. WANG Di and WANG Hao-liang conducted experiments and provided relevant data. DENG Guo-wei and CHEN Jie analyzed the results of experiments. TAN Chao-lin and DENG Guo-wei drafted the manuscript and revised the final version.

Conflict of interest

WANG Di, DENG Guo-wei, YANG Yong-qiang, CHEN Jie, WU Wei-hui, WANG Hao-liang, TAN Chao-lin declare that they have no conflict of interest.

References

[1] YIN Shuo, YAN Xing-chen, CHEN Chao-yue, JENKINS R, LIU Min, LUPOI R. Hybrid additive manufacturing of Al-Ti6Al4V functionally graded materials with selective laser melting and cold spraying [J]. Journal of Materials Processing Technology, 2018, 255: 650−655. DOI: 10.1016/j.jmatprotec.2018.01.015.

[2] HINOJOS A, MIRELES J, REICHARDT A, FRIGOLA P, HOSEMANN P, MURR L E, WICKER R B. Joining of Inconel 718 and 316 stainless steel using electron beam melting additive manufacturing technology [J]. Materials & Design, 2016, 94: 17−27. DOI: 10.1016/j.matdes.2016.01.041.

[3] ONUIKE B, HEER B, BANDYOPADHYAY A. Additive manufacturing of Inconel 718-copper alloy bimetallic

structure using laser engineered net shaping (LENS™) [J]. Additive Manufacturing, 2018, 21: 133−140. DOI: 10.1016/j.addma.2018.02.007.

[4] SHEN Chen, PAN Zeng-xi, CUIURI D, ROBERTS J, LI Hui-jun. Fabrication of Fe-FeAl Functionally graded material using the wire-arc additive manufacturing process [J]. Metallurgical and Materials Transactions B, 2015, 47(1): 763−772. DOI: 10.1007/s11663-015-0509-5.

[5] GURIANOV D A, KALASHNIKOV K N, OSIPOVICH K S, CHUMAEVSKII A V. Obtaining the bimetallic composition by the electron beam freeform fabrication [C]// IOP Conference Series: Materials Science and Engineering. 2019: 597: 012043. DOI: 10.1088/1757-899x/597/1/012043.

[6] ZHONG Yuan, RÄNNAR L E, WIKMAN S, KOPTYUG A, LIU Lei-feng, CUI Da-qing, SHEN Zhi-jian. Additive manufacturing of ITER first wall panel parts by two approaches: Selective laser melting and electron beam melting [J]. Fusion Engineering and Design, 2017, 116: 24−33. DOI: 10.1016/j.fusengdes.2017.01.032.

[7] FRAZIER W E. Metal additive manufacturing: A review [J]. Journal of Materials Engineering and Performance, 2014, 23(6): 1917−1928. DOI: 10.1007/s11665-014-0958-z.

[8] LEWANDOWSKI J J, SEIFI M. Metal additive manufacturing: A review of mechanical properties [J]. Annual Review of Materials Research, 2016, 46(1): 151−186. DOI: 10.1146/annurev-matsci-070115-032024.

[9] RAFI H K, KARTHIK N V, GONG Hai-jun, STARR T L, STUCKER B E. Microstructures and mechanical properties of Ti6Al4V parts fabricated by selective laser melting and electron beam melting[J] Journal of Materials Engineering and Performance, 2013, 22(12): 3872−3883. DOI: 10.1007/s11665-013-0658-0.

[10] BANDYOPADHYAY A, HEER B. Additive manufacturing of multi-material structures [J]. Materials Science and Engineering R: Reports, 2018, 129: 1−16. DOI: 10.1016/j.mser.2018.04.001.

[11] WEI Chao, SUN Zhe, HUANG Yi-he, LI Lin. Embedding anti-counterfeiting features in metallic components via multiple material additive manufacturing [J]. Additive Manufacturing, 2018, 24: 1−12. DOI: 10.1016/j.addma.2018.09.003.

[12] ZHANG Xiao-ji, CHUEH Yuan-hui, WEI Chao, SUN Zhe, YAN Ji-wang, LI Lin. Additive manufacturing of three-dimensional metal-glass functionally gradient material components by laser powder bed fusion with in situ powder mixing [J]. Additive Manufacturing, 2020, 33: 101113. DOI: 10.1016/j.addma.2020.101113.

[13] WEI Chao, SUN Zhe, CHEN Qian, LIU Zhu, LI Lin. Additive manufacturing of horizontal and 3D functionally graded 316L/Cu10Sn components via multiple material selective laser melting [J]. Journal of Manufacturing Science and Engineering, 2019, 141(8): 1−14. DOI: 10.1115/1.4043983.

[14] ZHANG Xiao-ji, WEI Chao, CHUEH Yuan-hui, LI Lin. An integrated dual ultrasonic selective powder dispensing platform for three-dimensional printing of multiple material metal/glass objects in selective laser melting[J]. Journal of Manufacturing Science and Engineering, 2019, 141(1): 011003. DOI: 10.1115/1.4041427.

[15] MEI Xin-liang, WANG Xiang-yu, PENG Yin-bo, GU Hong-yan, ZHONG Gao-yan, YANG Shou-feng. Interfacial characterisation and mechanical properties of 316L stainless steel/Inconel 718 manufactured by selective laser melting [J]. Materials Science and Engineering A, 2019, 758: 185−191. DOI: 10.1016/j.msea.2019.05.011.

[16] LIU Z H, ZHANG D Q, SING S L, CHUA C K, LOH L E. Interfacial characterisation of SLM parts in multi-material processing: Metallurgical diffusion between 316L stainless steel and C18400 copper alloy [J]. Materials Characterization, 2014, 94: 116−125. DOI: 10.1016/j.matchar.2014.05.001.

[17] CHEN Cai-yan, GU Dong-dong, DAI Dong-hua, DU Lei, WANG Rui, MA Cheng-long, XIA Mu-jian. Laser additive manufacturing of layered TiB_2/Ti6Al4V multi-material parts: Understanding thermal behavior evolution [J]. Optics & Laser Technology, 2019, 119. DOI: 10.1016/j.optlastec.2019.105666.

[18] DAI Dong-hua, GU Dong-dong, POPRAWE R, XIA Mu-jian. Influence of additive multi-layer feature on thermodynamics, stress and microstructure development during laser 3D printing of aluminum-based material [J]. Science Bulletin, 2017, 62(11): 779−787. DOI: 10.1016/j.scib.2017.05.007.

[19] BOBBIO L D, OTIS R A, BORGONIA J P, DILLON R P, SHAPIRO A A, LIU Zi-kui, BEESE A M. Additive manufacturing of a functionally graded material from Ti-6Al-4V to Invar: Experimental characterisation and thermodynamic calculations [J]. Acta Materialia, 2017, 127: 133−142. DOI: 10.1016/j.actamat.2016.12.070.

[20] TOMASHCHUK I, SALLAMAND P, CICALA E, PEYRE P, GREVEY D. Direct keyhole laser welding of aluminum alloy AA5754 to titanium alloy Ti6Al4V [J]. Journal of Materials Processing Technology, 2015, 217: 96−104. DOI: 10.1016/j.jmatprotec.2014.10.025.

[21] DEMIR A G, PREVITALI B. Multi-material selective laser melting of Fe/Al-12Si components [J]. Manufacturing Letters, 2017, 11: 8−11. DOI: 10.1016/j.mfglet.2017.01.002.

[22] SING S L, LAM L P, ZHANG D Q, LIU Z H, CHUA C K. Interfacial characterisation of SLM parts in multi-material processing: Intermetallic phase formation between AlSi10Mg and C18400 copper alloy [J]. Materials Characterization, 2015, 107: 220−227. DOI: 10.1016/j.matchar.2015.07.007.

[23] ONUIKE B, BANDYOPADHYAY A. Additive manufacturing of Inconel 718–Ti6Al4V bimetallic structures [J]. Additive Manufacturing, 2018, 22: 844−851. DOI: 10.1016/j.addma.2018.06.025.

[24] KOOPMANN J, VOIGT J, NIENDORF T. Additive manufacturing of a steel–ceramic multi-material by selective laser melting [J]. Metallurgical and Materials Transactions B, 2019, 50(2): 1042−1051. DOI: 10.1007/s11663-019-01523-1.

[25] WEI Chao, LI Lin, ZHANG Xiao-ji, CHUEH Yuan-hui. 3D printing of multiple metallic materials via modified selective laser melting [J]. CIRP Annals, 2018, 67(1): 245−248. DOI: 10.1016/j.cirp.2018.04.096.

[26] TAN Chao-lin, ZHANG Xin-yue, DONG Dong-dong, ATTARD B, WANG Di, KUANG Min, MA Wen-you, ZHOU Ke-song. In-situ synthesised interlayer enhances bonding

strength in additively manufactured multi-material hybrid tooling [J]. International Journal of Machine Tools and Manufacture, 2020, 155: 103592. DOI: 10.1016/j.ijmachtools.2020.103592.

[27] ZHANG Ming-kang, YANG Yong-qiang, WANG Di, SONG Chang-hui, CHEN Jie. Microstructure and mechanical properties of CuSn/18Ni300 bimetallic porous structures manufactured by selective laser melting [J]. Materials & Design, 2019, 165: 107583. DOI: 10.1016/j.matdes.2019.107583.

[28] CHEN Jie, YANG Yong-qiang, SONG Chang-hui, ZHANG Ming-kang, WU Shi-biao, WANG Di. Interfacial microstructure and mechanical properties of 316L /CuSn10 multi-material bimetallic structure fabricated by selective laser melting [J]. Materials Science and Engineering A, 2019, 752: 75−85. DOI: 10.1016/j.msea.2019.02.097.

[29] CARTER L N, MARTIN C, WITHERS P J, ATTALLAH M M. The influence of the laser scan strategy on grain structure and cracking behaviour in SLM powder-bed fabricated nickel superalloy [J]. Journal of Alloys and Compounds, 2014, 615: 338−347. DOI: 10.1016/j.jallcom.2014.06.172.

[30] TAN Chao-lin, WANG Di, MA Wen-you, CHEN Yao-rong, CHEN Shi-jie, YANG Yong-qiang, ZHOU Ke-song. Design and additive manufacturing of novel conformal cooling molds [J]. Materials & Design, 2020, 196: 109147. DOI: 10.1016/j.matdes.2020.109147.

[31] WANG Rui, GU Dong-dong, XI Li-xia, LIN Kai-jie, GUO Meng, ZHANG Hong-mei. Selective laser melted TiB2/Ti6Al4V graded materials and first-principle calculations [J]. Materials Letters, 2019, 254: 33−36. DOI: 10.1016/j.matlet.2019.07.015.

[32] YAN Lei, CHEN Yi-tao, LIOU F. Additive manufacturing of functionally graded metallic materials using laser metal deposition [J]. Additive Manufacturing, 2020, 31: 100901. DOI: 10.1016/j.addma.2019.100901.

[33] TAN Chao-lin, ZHOU Ke-song, KUANG Tong-chun. Selective laser melting of tungsten-copper functionally graded material [J]. Materials Letters, 2019, 237: 328−331. DOI: 10.1016/j.matlet.2018.11.127.

[34] TAN Chao-lin, ZHOU Ke-song, MA Wen-you, MIN Liu. Interfacial characteristic and mechanical performance of maraging steel-copper functional bimetal produced by selective laser melting based hybrid manufacture [J]. Materials & Design, 2018, 155: 77−85. DOI: 10.1016/j.matdes.2018.05.064.

[35] MAGNABOSCO I, FERRO P, BONOLLO F, ARNBERG L. An investigation of fusion zone microstructures in electron beam welding of copper–stainless steel [J]. Materials Science and Engineering A, 2006, 424(1, 2): 163−173. DOI: 10.1016/j.msea.2006.03.096.

[36] TEY C F, TAN Xi-peng, SING S L, YEONG W Y. Additive manufacturing of multiple materials by selective laser melting: Ti-alloy to stainless steel via a Cu-alloy interlayer [J]. Additive Manufacturing, 2020, 31: 100970. DOI: 10.1016/j.addma.2019.100970.

[37] TALIC B, HENDRIKSEN P V, WIIK K, LEIN H L. Thermal expansion and electrical conductivity of Fe and Cu doped $MnCo_2O_4$ spinel [J]. Solid State Ionics, 2018, 326: 90−99. DOI: 10.1016/j.ssi.2018.09.018.

(Edited by HE Yun-bin)

中文导读

激光选区熔化成型多层结构功能梯度材料的界面组织和性能

摘要：功能梯度材料(FGM)可以在零件的不同区域定制其特性，例如耐磨性、耐腐蚀性和环境适应性。激光选区熔化(SLM)在制造FGM上具有出色表现，故本文采用SLM技术制备了316L/CuSn10/18Ni300/CoCr四种材料的FGM，研究了FGM的微观结构和性能，以揭示SLM加工参数对缺陷的影响。在316L/CuSn10界面处发现了许多微裂纹，这些裂纹自316L区域的熔合边界萌生并沿成型方向延伸。18Ni300/CoCr熔合区的弹性模量和纳米硬度显着下降，低于18Ni300和CoCr区域的弹性模量和纳米硬度。铁元素和铜元素在316L/CuSn10熔合区充分扩散，而CuSn10/18Ni300和18Ni300/CoCr熔合区中的元素则表现出明显的梯度转变。与其他区域相比，CuSn10/18Ni300界面和CuSn10区域具界面结合区域有明显的尺寸膨胀。最后，本文重点讨论了316L/CuSn10界面处的材料熔合和裂纹形成的机理。发现仅通过改变316L和CuSn10的沉积顺序就可以成型没有宏观裂纹的FGM，这为FGM的增材制造提供了指导。

关键词：激光选区熔化；多层结构功能梯度材料；界面表征；裂纹缺陷；力学性能